THE RISE OF GNSS REFLECTOMETRY FOR EARTH REMOTE SENSING

Cinzia Zuffada, Zhijin Li, Son V. Nghiem, Steve Lowe, Rashmi Shah
Jet Propulsion Laboratory, California Institute of Technology, USA

Maria Paola Clarizia
University of Michigan at Ann Arbor, USA

Estel Cardellach
Institut De Ciencies De L'Espai's, Barcelona, Spain

ABSTRACT

The Global Navigation Satellite System (GNSS) reflectometry, i.e. GNSS-R, is a novel remote-sensing technique first published in [1] that uses GNSS signals reflected from the Earth's surface to infer its surface properties such as sea surface height (SSH), ocean winds, sea-ice coverage, vegetation, wetlands and soil moisture, to name a few. This communication discusses the scientific value of GNSS-R to (a) furthering our understanding of ocean mesoscale circulation toward scales finer than those that existing nadir altimeters can resolve, and (b) mapping vegetated wetlands, an emerging application that might open up new avenues to map and monitor the planet's wetlands for methane emission assessments. Such applications are expected to be demonstrated by the availability of data from GEROS-ISS, an ESA experiment currently in phase A [2], and CyGNSS [3], a NASA mission currently in development. In particular, the paper details the expected error characteristics and the role of filtering played in the assimilation of these data to reduce the altimetric error (when averaging many measurements).

***Index Terms*—** GNSS, sea surface topography, mesoscale ocean, wetland mapping

1. INTRODUCTION

The GNSS-R measurement concept takes advantage of the ever-increasing number of GNSS transmitting satellites, and relies on the exploitation of the signals after they have been scattered off the Earth surface and are collected by one or more specially designed Global Positioning System (GPS) receiver(s) forming a bistatic (or multistatic) radar. By exploiting signals of opportunity and requiring relatively simple instrumentation for the receiver, it offers a cost-effective way to provide many randomly distributed measurements with broad-area global coverage and rapid revisit time in all weather conditions, although in some cases at degraded accuracy compared to a monostatic radar. The technique has been demonstrated in a number of field experiments with GPS receivers on towers, airplanes, balloons, and satellites [3-8].

The received reflected signals are cross-correlation products, collecting contributions scattered from a broad area around the surface specular reflection point (SP), presented as waveforms of power versus delay, or power versus delay and Doppler. From these, either (or both) altimetric or scatterometric measurements can be derived. GNSS-R altimetry uses the difference in arrival time at the receiver between the direct and reflected (along the leading edge) signals to measure the surface height (at and around the specular reflection point) relative to the receiver. This, combined with the receiver location deduced from GPS, gives measurements of the surface topography. GNSS-R scatterometry uses features of the returned signal pulse shape such as peak power, fall-time or power versus Doppler to deduce surface properties. Example scatterometric GNSS-R measurements include sea-surface roughness, ocean winds, soil moisture, wetland extension and sea ice age. A key innovation of the GNSS-R scatterometry is that the bistatic received signal from the reflection and scattering in the forward direction is much stronger than the backscatter configuration of monostatic radar such as synthetic aperture radars or monostatic scatterometers. This major difference may offer a new method to advance the current capability for certain applications such as wetland mapping. As a specific application of wind scatterometry, the CyGNSS NASA mission will measure hurricane winds with a constellation of eight small satellites.

2. ALTIMETRY ERROR - PRECISION

The GNSS-R instrument (receiver plus up- and down-looking antenna systems) collects scattering contributions in the forward scattering direction from an area around the SP, determined by delay and Doppler filters for surface selectivity by coherent integration in the receiver and signal autocorrelation properties. Each cross-correlation waveform is typically incoherently summed over 1 sec, to yield a cleaner leading edge (higher signal-to-noise ratio (SNR)). A number of different algorithms have been developed to find the optimal point along the leading edge from which to reference the delay. Specifically, they are referred to as the Leading Edge Derivative (LED) [9-10], the leading Edge Half Point (HALF) [11], and the Waveform Curve Fitting applied to either the leading edge or the complete delay waveform. Here we report the results from waveforms generated by CyGNSS End-to-End Simulator (E2ES) in conjunction with C/A GPS code [12]. Specifically, the LED, HALF and Waveform Curve Fitting algorithms were applied to GPS-R data simulated with parameters summarized in Table 1.

Specifically, the LED and HALF have been implemented on both delay waveforms (i.e. at zero Doppler frequency), and on Integrated Delay Waveforms (IDW) that are obtained by integrating the Delay-Doppler Map along the full range of Doppler frequencies. Here we illustrate the results for the algorithm that

delivers the best performance: the HALF algorithm applied to delay waveforms. Furthermore, the HALF algorithm has been tested for different fractions of the peak power, in an attempt to keep the SSH precision as low as possible while maintaining the bias in the retrieval algorithm reasonably constant with respect to geometrical and geophysical (i.e. wind speed) parameters.

PARAMETER	VALUE
CARRIER FREQUENCY	L1 (1575.42 MHz)
CODE	COARSE/ACQUISITION (C/A)
SPECKLE NOISE / THERMAL NOISE	ON
GEOMETRY	INCIDENCE ANGLE= [1° 10° 20° 31° 40° 50°] AZIMUTH ANGLE = 70°
WIND SPEED [m/s]	5, 10, 15, 20, 30
WIND DIRECTION	0°
NUMBER OF REALIZATIONS (FOR EACH GEOMETRY/WIND SPEED PAIR)	500
MEAN SEA LEVEL [m]	0
COHERENT/INCOHERENT INTEGRATION TIME [s]	0.001, 1
RX BANDWIDTH/SAMPLING RATE [MHz]	5, 16.367
MAX ANTENNA GAIN [dBi]	14.7, 20.3
GPS TX POWER [dB]	14.25
ATMOSPHERIC LOSS	Not assumed
DDM RESOLUTION [chip/Hz]	0.25 / 500

Table 1. Parameters used for the generation of DDMs from the CYGNSS E2ES.

An optimal peak fraction of the delay waveform peak power was identified in this case as 0.5. The SSH precision is then computed from the specular point delay using equation (12) in [10], and it is shown in Figure 1. The results for CyGNSS geometries have been extended to the case of antenna gain higher than the CyGNSS peak gain (~14.7 dBi), up to the typical peak gains envisaged for systems like PARIS or GEROS-ISS (20.3 dBi). The SSH precision for the CyGNSS peak gain oscillates between 1.9 m for a low wind speed, and 3.1 m for a high wind speed. For a higher peak gain of 20.3 dBi, the effect of the wind speed is weaker, and the SSH precision varies within a narrower range between 1.3 m and 1.7 m.

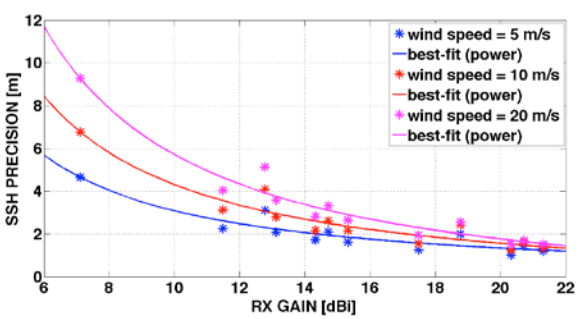

Figure 1. SSH precision in meters, versus receiver antenna gain in dBi. The stars represent estimations from CYGNSS DDMs simulated for three different wind speed values (5, 10 and 20 m/s). The continuous lines are best-fit power functions.

The SSH bias caused by the retrieval algorithm is calculated from the SP delay bias, using simple geometrical considerations, and the knowledge of transmitter, receiver and specular position on the WGS84 ellipsoid. The SSH bias is shown as a function of wind speed in Figure 2. A small amount of variability of the bias with respect to wind speed remains, evidence that a non-perfect retrieval or a-priori knowledge of the wind speed will cause a small error in SSH estimation. However, the variability decreases for increasing gain of the receiving antenna.

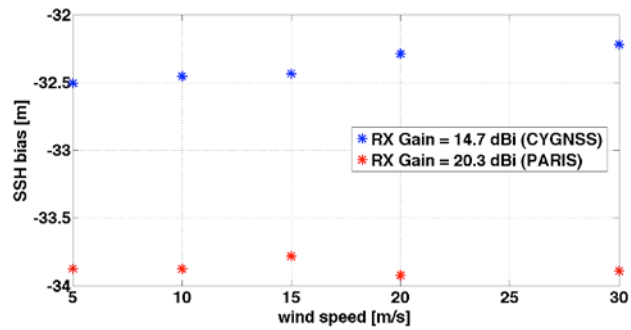

Figure 2. Altimetric SSH bias as a function of wind speed, for a fixed CyGNSS geometry (specular point very close to the antenna boresight) and both CyGNSS and PARIS peak antenna gain.

3. ALTIMETRY ERROR - SYSTEMATICS

In this section, we describe the various factors that affect the accuracy of altimetric measurements for spaceborne instruments. The precision, which accounts for thermal noise and speckle, can range from 20 - 90 cm (per 100 km) depending on geometry, GNSS signal, SNR [13] and processing technique. In addition to the thermal and speckle noise, the precision will also be affected by the bias in the retrieval algorithm, bringing the overall precision error range to 50-150 cm. The estimate of the ionospheric (and tropospheric) propagation effect ranges from 20-40 cm as derived from radio occultation heritage, assuming that the receiver operates at L1, L2 and L5 frequencies and a linear combination of the signal can be formed to reduce the ionospheric noise [6]. Errors caused by the surface scattering component or Sea-State Bias comprise electromagnetic bias, skewness bias, and tracking bias and can range between 5 – 15 cm depending on the geometry [6; 14]. The orbit and instrument (antenna phase center) component of the error are estimated from those manifesting in traditional nadir altimetry but accounting for the angular dependence of the GNSS-R measurement geometry, and can range between 5-10 cm [6; 13; 14]. The oceanographic error caused by tides, geoid, and inverted barometer that exists in traditional altimetry should also be applied after accounting for the bistatic geometry of GNSS-R. An estimate of this from traditional altimetry is of the order of a few centimeters.

After examining all the error components, it is noted that the precision, with its characteristics of random error with zero mean, is the dominant component; we will refer solely to the precision in the next Section when discussing how to use the GNSS-R sea surface topography data in data assimilation schemes (based on Optimal Interpolation) and assess its impact in resolving high spatial and temporal resolution features such as mesoscale eddies. Basically, the precision will dictate how many independent measurements are required to beat down the error to a level where resolution of features of desired scales is possible, assuming that the systematics can be accounted for.

4. MESOSCALE OCEANOGRAPHY

While the 1-spatial dimensional SSH spectrum is well sampled by traditional nadir altimetry, the 3-dimensional space-time spectrum of mesoscale SSH features is not as well known due to the nadir altimetry's sampling characteristics: 6-7 km along-track, but ~ 300 km between tracks at the equator with a 10 day sampling pattern, assuming a single altimeter. Even two altimeters leave gaps of about 150 km at the Equator every 10 days, which is the time it takes a mesoscale eddy to move about 40 km and therefore disappear between tracks (eddies typically drift westward at speed of ~5 cm/s at 25° latitude, and more than 15 cm/s at 10° latitude). A measurement that can fill in such gaps is needed to better understand the mesoscale spectrum. Sea energy at wavelengths shorter than 200 km is key to understanding forward and reverse energy transfers: from large to small scales or from small to large scales in both space and time, a fundamental challenge in making ocean circulation models realistic in closing the energy budget and the representation of kinetic energy dissipation.

A multistatic GNSS-R altimeter system may produce 100 simultaneous ocean height measurements, one to two orders of magnitude more than a traditional altimeter, based on today's number of GNSS transmitters. Even with large precision errors, this large number of measurements offers the potential of resolving mesoscale circulation through averaging, improving the height precision over various spatial and temporal scales depending on the science application. For a spatial grid size of 50 km and a time length of 3 days, the RMSE of the average of measurements with 50 cm 1-sec precision ranges from 0.08 m at high latitudes to 0.18 m near the equator. This range of RMSE shows the potential that a combination of three to four receivers may produce SSH measurements that have an error less than 0.05 m and thus resolve mesoscale circulations down to 50 km and 3 days, essentially the entire spectra of mesoscales. Further, GNSS-R measurements are homogeneously distributed with broad-area global coverage and are acquired in all weather conditions.

In the past decade, a host of advanced data mapping and data assimilation methodologies has been developed, known as optimal estimation. Among them are commonly used Optimal Interpolation (OI), Kalman filter/smoother and three/four-dimensional variational data assimilation (3/4DVar). These advanced methodologies provide powerful techniques to exploit the potential of GNSS-R measurements in resolving the spectra of mesoscales down to 50 km.

Greenslade *et al.* [15] assessed the effective spatial/temporal resolution of OI maps based on the data from a number of traditional altimeters by seeking a smoothing scale such that the mapping errors were relatively homogeneous in space. The resulting smooth scales were 6x6 degrees for a single altimeter and 3x3 degrees for two altimeters. Chelton *et al.* [16] were able to track eddies of 200 km diameter across the global oceans in two dimensional maps based on 2 altimeters using the OI mapping, but smaller eddies or a more continuous tracking were not possible.

To assess the impact of GNSS-R altimetry data on mapped mesoscale circulation, it is necessary to conduct similar mapping analyses, but following the Observing System Simulation Experiment (OSSE) framework. There a model simulation, known as a "nature run" or "ground truth", serves as a surrogate for the true ocean state. From this nature run, one can produce simulated observations. A variety of studies can then be carried out with simulated GNSS-R data, corresponding to assuming a certain number of receivers and realistically simulated errors. The sampled data is also known as "synthetic measurements". Applying the OI mapping to the synthetic measurements, we can evaluate the resulting observed spectra to show under what observational scenarios the eddy wavenumbers and frequencies can be resolved appropriately. This analysis method can also be used to assess tradeoffs in spatial resolution, temporal revisit, mapped SSH error, and so on.

OSSEs are more often used with data assimilation. Different from data mapping, data assimilation is a methodology for the integration of available observations into a dynamical model to produce fields. With OSSEs, a model is initialized with a state different from the nature run. Using the experiments with and without assimilation of GNSS-R altimetry data, we can assess its impact on the model simulation.

Figure 3 presents a preliminary OSSE. A nature run was first performed to simulate the large Loop Current eddy in the Gulf of Mexico. Synthetic observations of SSH are then obtained from this run using sampling characteristics from six simulated spaceborne receivers. A 50-cm Gaussian error is added to the synthetic SSHs. A control run is performed with an initial condition offset by three months from the nature run, thus significantly altering the structure of the Loop Current and the eddy. The synthetic observations of SSHs are assimilated into the control run using a three-dimensional variational data assimilation scheme [17]. The assimilation of GNSS-R measurements reproduces the loop ring shedding. This OSSE indicates that GNSS-R could have a significant impact on the eddy shedding prediction that is a long known challenge.

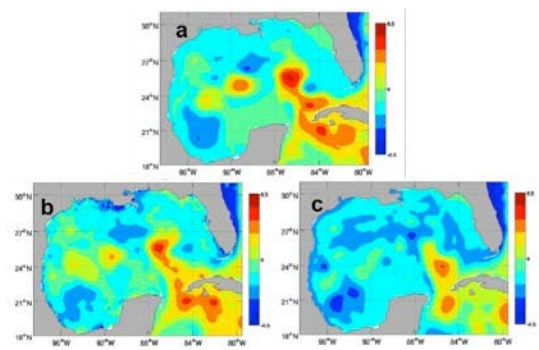

Figure 3. Observing System Simulation Experiment (OSSE). The "true" state is shown in (a), the state with the assimilation of GNSS-R SSHs in (b), and the state without data assimilation in (c). The assimilation of GNSS-R altimetry data reproduces the loop ring in the Gulf of Mexico. SSH is in m.

5. WETLANDS MAPPING

Wetland dynamics is a key driver of changes in both atmospheric methane and terrestrial water storage. The Intergovernmental Panel on Climate Change's Fifth Assessment Report (IPCC AR5) highlights the role of wetlands as a key driver of methane emission, which is more than one order of magnitude stronger than carbon dioxide as a greenhouse gas in the centennial time scale, yet a complete and consistent map of global wetlands still needs to be obtained as the Ramsar Convention [18] calls for a wetlands inventory and impact assessment.

GNSS-R bistatic scatterometry uses features of the returned signal pulse shape such as peak power and/or trailing edge to deduce surface properties, which are relevant to inundated wetland mapping. Bistatic signatures in the forward direction are strongly dependent on the permittivity of the land surface medium [19]. On

inundated wetlands, the kind of wetlands pertaining to the anaerobic metabolism for CH_4 emission, the permittivity of water in liquid phase can be an order of magnitude larger than that of dry land [20]. As such, bistatic scatterometery signals from inundated wetlands are much stronger than those from dry land, thus allowing a distinctive identification of the wetlands. Moreover, GNSS-R signals can have a better penetration through the vegetation cover because GNSS frequencies are typically low such as L band or lower, compared to C, X, Ku, and Ka bands of many past, current, and future monostatic radar systems.

Recently, a feasibility study to measure and monitor wetland dynamics using GNSS-R observations has been conducted based on available data from an aircraft field campaign conducted over the Catalonia wetland of the Ebro delta in Spain. Initial results from this flight campaign have demonstrated that strong signatures of the wetland under a thick vegetation canopy of rice plants can be observed with reflected GNSS signals, which are distinctive from dry-land signatures (Figure 4) and thus demonstrating the capability of GNSS-R for wetland mapping.

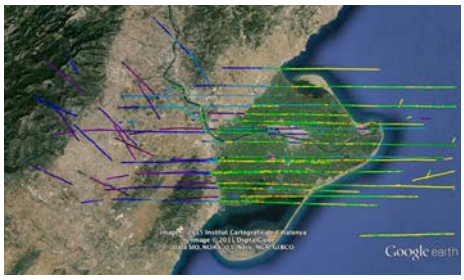

Figure 4. Reflected peak power measured over rice fields in Spain Ebre delta in July 2005 with Gold GPS s/w receiver (data courtesy of [14].)

It is noted that the delay waveforms over ocean have the typical broadened shape associated with incoherent scattering, whereas those over wetlands have the triangular shape consistent with coherent scattering (Figure 5). The ratio of reflected/direct power over rice fields is about the same as the ratio of reflected/direct power over ocean.

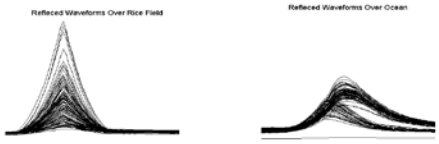

Figure 5. On the left are Waveforms reflected from rice fields (coherent return) and on the right are Waveforms reflected from ocean (incoherent returns).

6. ACKNOWLEDGEMENTS

The research was performed in part by the Jet Propulsion Laboratory under contract with NASA. Dr. Clarizia was supported by a subcontract from JPL to the University of Michigan. The support from JPL Advance Concepts for Wetland Science in noted.

7. REFERENCES

[1] Martín-Neira, M. (1993): A passive reflectometry and interferometry system (PARIS): Application to ocean altimetry. *ESA Journal*, *17*, 331-355.

[2] Wickert, Jens, Ole Baltazar Andersen, George Beyerle, Estel Cardellach, Bernard Chapron, Christoph Förste, Christine Gommenginger et al. (2013): GEROS-ISS: GNSS Reflectometry, Radio Occultation and Scatterometry Onboard the International Space Station, In *4th International Colloquium Scientific and Fundamental Aspects of the Galileo Programme*.

[3] Ruf, C., M. Unwin, J. Dickinson, R. Rose, D. Rose, M. Vincent, and A. Lyons (2013): CYGNSS: Enabling the Future of Hurricane Prediction [Remote Sens. Satellites]. *Geosci, Remote Sens. Mag., IEEE*, *1*(2), 52-67.

[4] Lowe, S. T., C. Zuffada, Y. Chao, P. Kroger, L. E. Young, and J. L. LaBrecque (2002b): 5-cm-Precision aircraft ocean altimetry using GPS reflections. *Geophysical Research Letters*, *29*(10), 13-11-13-14.

[5] Rius, A., E. Cardellach, and M. Martin-Neira (2010): Altimetric analysis of the sea-surface GPS-reflected signals. *Geoscience and Remote Sensing, IEEE Transactions on*, *48*(4), 2119-2127.

[6] Martín-Neira, M., S. D'Addio, C. Buck, N. Floury, and R. Prieto-Cerdeira (2011): The PARIS ocean altimeter in-orbit demonstrator. *Geoscience and Remote Sensing, IEEE Transactions on*, *49*(6), 2209-2237.

[7] Lowe, S. T., J. L. LaBrecque, C. Zuffada, L. J. Romans, L. E. Young, and G. A. Hajj (2002a): First spaceborne observation of an Earth-reflected GPS signal. *Radio Science*, *37*(1), 7-1-7-28.

[8] Gleason, S., S. Hodgart, Y. Sun, C. Gommenginger, S. Mackin, M. Adjrad, and M. Unwin (2005): Detection and processing of bistatically reflected GPS signals from low earth orbit for the purpose of ocean remote sensing. *Geosci. Remote Sens., IEEE Trans. on*, *43*(6), 1229-1241.

[9] Hajj, G.A., and C. Zuffada (2003): Theoretical description of a bistatic system for ocean altimetry using the GPS signal, *Radio Science*, 38(5):1089.

[10] Rius, A., Cardellach, E., Martín-Neira, M. (2010), Altimetric Analysis of the Sea-Surface GPS-Reflected Signals, *IEEE Transactions on Geoscience and Remote Sensing*, 48, 4, pp. 2119 – 2127.

[11] Cardellach, E., Rius, A., Martín-Neira, M., Fabra, F., Nogués-Correig, O., Ribó, S., Kainulainen, J., Camps, A., D Addio, S. (2013): Consolidating the Precision of Interferometric GNSS-R Ocean Altimetry using Airborne Experimental Data, *IEEE Transactions on Geoscience and Remote Sensing*.

[12] O'Brien, A., S. Gleason, J. Johnson, C. Ruf (2014): The End-to-End Simulator for the Cyclone GNSS (CYGNSS) Mission, *IEEE Transactions on Geoscience and Remote Sensing*, in review.

[13] Camps, A.; Hyuk Park; Valencia i Domenech, E.; Pascual, D.; Martin, F.; Rius, A.; Ribo, S.; Benito, J.; Andres-Beivide, A.; Saameno, P.; Staton, G.; Martin-Neira, M.; D'Addio, S.; Willemsen, P. (2014): "Optimization and Performance Analysis of Interferometric GNSS-R Altimeters: Application to the PARIS IoD Mission," *Selected Topics in Applied Earth Observations and Remote Sens., IEEE J. of*, vol.7, no.5, pp.1436-1451.

[14] Cardellach, E., Fabra, F., Nogués-Correig, O., Oliveras, S., Ribó, S., Rius, A. (2011): GNSS-R ground-based and airborne campaigns for Ocean, Land, Ice and Snow techniques: application to the GOLD-RTR datasets, Radio Science, 46, RS0C04.

[15] Greenslade, D., D. Chelton, M. Schlax (1997): The Midlatitude Resolution Capability of Sea Level Fields Constructed from Single and Multiple Satellite Altimeter Datasets, *J. Atmosph Oceanic Techn*., 849-870.

[16] Dudley B. Chelton, Michael G. Schlax, Roger M. Samelson (2011): Global observations of nonlinear mesoscale eddies, Progress in Oceanography 91 167–216.

[17] Li, Z., Chao, Y., McWilliams, J. C., and Ide, K. (2008): A three-dimensional variational data assimilation scheme for the Regional Ocean Modeling System, J. Atmos. Oceanic Tech., 25, 2074-2090.

[18] Ramsar Convention (2015), *The Ramsar Convention on Wetlands*, http://www.ramsar.org/, accessed May 2015.

[19] Ulaby, F. T., R. K. Moore, and A. K. Fung (1986), *Microwave Remote Sensing Active and Passive*, Vol. III, From Theory to Applications, Artech House, Dedham, Massachusetts.

[20] Tsang, L., J. A. Kong, and R. T. Shin (1985), *Theory of Microwave Remote Sensing*, John Wiley & Sons, New-York.